

ENGINEERING

Programmable aniso-electrodeposited modular hydrogel microrobots

Zhiqiang Zheng^{1,2}, Huaping Wang^{1,3*}, Sinan Ozgun Demir², Qiang Huang^{3,4*}, Toshio Fukuda⁴, Metin Sitti^{2,5,6*}

Systems with programmable and complex shape morphing are highly desired in many fields wherein sensing, actuation, and manipulation must be performed. Living organisms use nonuniform distributions of their body structural composition to achieve diverse shape morphing, motion, and functionality. However, for the micro-robot fabrication, these designs often involve complicated robotic architectures requiring time-consuming and arduous fabrication processes. This paper proposes a single-step aniso-electrodeposition method for fabricating modular microrobots (MMRs) with distinct functions in each modular segment. By programming the electric field, the microscale stripe-shaped structure can be endowed with diverse shape-morphing capabilities, such as spiraling, twisting, bending, and coiling. The proposed fabrication method can develop MMRs with multiple independent modules onto which cells, drugs, and magnetic nanoparticles can be loaded to achieve multifunctionality. Thus, MMRs can perform multiple tasks, such as propulsion, grasping, and object delivery, simultaneously under magnetic control and ionic and pH stimuli.

INTRODUCTION

Living creatures, from mammals to microorganisms, have modular designs that allow them to perform complex motions and multiple functions (1). Inspired by living organisms, conventional rigid robots with modular designs have been developed and can perform various functions, such as walking (2), grasping (3), and sensing. In the past decade, soft microrobots have attracted significant attention owing to their shape programmability, physical adaptability, and safer human interaction (4, 5). However, it is generally challenging to integrate multiple functions, such as sensing, shape morphing, and decision-making, into a single soft microrobot (6–8). Although many microswimmers and micromachines have achieved actuation or shape morphing in response to temperature (9–12), light (13–16), pH (17–19), and magnetic and electric fields (20–26), modular designs with distinct compositions and functions in each module are still lacking in the soft microbotics field.

Many methods for fabricating shape-morphing soft microrobots, such as photolithography (27–30), four-dimensional (4D) printing (31, 32), molding (33, 34), and laser micromachining (11, 35, 36), have been proposed to enable bending or twisting microstructures. These moving structures have typically uniform material composition and shape-morphing capability, which restricts them to have multifunctional modular designs (37, 38). These fabrication methods can only achieve complex shape morphing by combining tedious manufacturing, multiple substructure design,

and multistep processing. For example, 4D printing still follows the rules of a bilayer structure, whereby shape morphing is generated through the anisotropic swelling of the materials in each layer. This means that a transformable substructure should have an isotropic architecture, homogeneous composition, and single transformation (39, 40). Hence, to create multifunctional shape-morphing microrobots, a modularized fabrication method should be developed to endow the distinct modules of an integrated modular soft microrobot with varying transformation and composition.

To develop a multitasking soft modular microrobot (MMR), we propose an anisotropic electrodeposition method for single-step fabrication of soft microrobot modules with distinct 3D conformations and compositions (Fig. 1). Aniso-electrodeposition uses a programmable anisotropic 3D electric field to embed complex heterogeneous cross-linking densities into hydrogel networks, which allows each robot segment to perform a distinct shape morphing (bending, twisting, and coiling) and respond to external stimuli, such as pH, ions, and magnetic fields. By applying droplets with different compositions to respective target regions, aniso-electrodeposition can simultaneously generate up to three segments with distinct composition and shape-morphing behaviors within a few seconds. Finite element analysis (FEA) can be established to program and predict the shape morphing of the electrodeposited structures. To demonstrate their programmable and modularized shape-morphing ability, these shape-morphing structures have been used to develop MMRs with stripe, cross, and claw shapes. Among them, the claw-shaped MMRs for sensing and payload delivery use a propulsion module containing magnetic particles to achieve controllable locomotion and adaptive shape morphing and a functional module containing the biofunctional cells or dyes required in specific tasks, such as tissue regeneration and drug delivery. The propulsion module can accurately deliver a bio-compatible functional module to the target area, where the functional module releases cells or dyes through physical contact with the target area. Subsequently, the propulsion module can be disassembled and removed. The proposed aniso-electrodeposition

Copyright © 2022
The Authors, some
rights reserved;
exclusive licensee
American Association
for the Advancement
of Science. No claim to
original U.S. Government
Works. Distributed
under a Creative
Commons Attribution
NonCommercial
License 4.0 (CC BY-NC).

¹Intelligent Robotics Institute, School of Mechatronical Engineering, Beijing Institute of Technology, Beijing 100081, China. ²Physical Intelligence Department, Max Planck Institute for Intelligent Systems, Stuttgart 70569, Germany. ³Key Laboratory of Biomimetic Robots and Systems, Beijing Institute of Technology, Ministry of Education, Beijing 100081, China. ⁴Beijing Advanced Innovation Center for Intelligent Robots and Systems, Beijing Institute of Technology, Beijing 100081, China. ⁵Institute for Biomedical Engineering, ETH Zürich, Zürich 8092, Switzerland. ⁶School of Medicine and College of Engineering, Koç University, Istanbul 34450, Turkey.

*Corresponding author. Email: wanghuaping@bit.edu.cn (H.W.); qhuang@bit.edu.cn (Q.H.); sitti@is.mpg.de (M.S.)

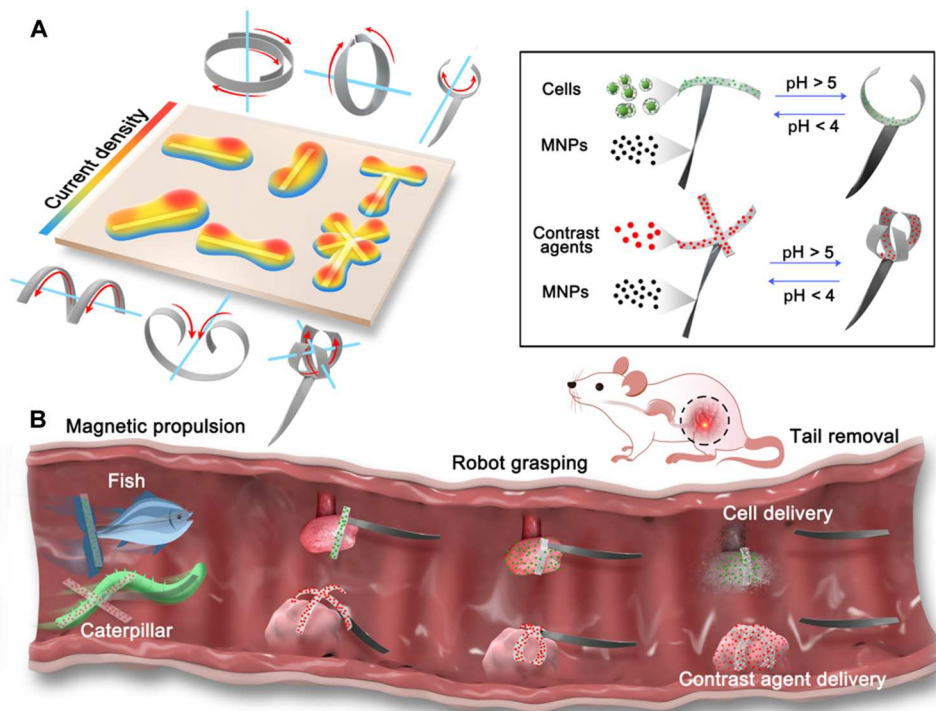


Fig. 1. Principle of aniso-electrodeposition method and illustration of the aniso-electrodeposited MMRs. (A) In aniso-electrodeposition, a 3D electric field is used to embed complex heterogeneous cross-link density into hydrogel networks to generate different types of shape morphing. **(B)** Schematic illustration of MMRs in the rat gastrointestinal tract. Through aniso-electrodeposition, drugs, contrast agents, cells, and magnetic nanoparticles (MNPs) can be loaded onto the different hydrogel microstructure modules of the MMR. Under magnetic control, there are two locomotion modes, fish-like and caterpillar-like locomotion, which allow the microrobots to move toward and self-grasp the target, release the payload, and remove the magnetic modules after payload delivery.

method offers a new direction toward developing next-generation microrobots that are safer, softer, smarter, more efficient, and more integrated.

RESULTS

Hydrogel microstructure shape-morphing parameters

Alginate hydrogels are gelled by ionic cross-linking through combination of alginate with divalent cations, which causes the coordination of divalent ions with four carboxyl groups to form an egg-box arrangement that shrinks the gel network. An inverse phenomenon has been observed in alginate hydrogels, because the functional acid groups (for example, $-\text{COO}^-$) undergo protonation at higher pH values ($\text{pH} > 5$) or react with monovalent cations, which leads to the absorption of water and triggers a loosen gel network (41). To illustrate the principle of shape morphing, we fabricated a basic stripe structure in the horizontal and vertical directions along the electric field (Fig. 2A) based on the electrodeposition setup illustrated in the fig. S1. The simulation results reveal that the electric field can generate both in-plane difference and out-of-plane gradients that lead to the nonuniform 3D distribution of the current density. The nonuniform current density results in the nonuniform distribution of the cross-linking density, which further causes the gradient of the swelling coefficient. The gradient of the swelling coefficients in the structure is the main driving force behind the deformation of the heterogeneous hydrogel structures. The force imbalance between different parts generates torque, which results in the bending and deformation of the hydrogel microstructure

toward the direction in which the highest amount of strain energy is released. In a horizontal microstructure, there is a large gradient along the long axis (electric field). Therefore, the horizontal microstructure exhibits curling along the long axis after shrinkage (movie S1). However, in a vertical microstructure, the current density is inhomogeneously distributed throughout the 3D architecture. Therefore, the vertical microstructure can perform a Möbius ring-shaped deformation as shown in movie S2.

To illustrate the electric field gradient, we fabricated the stripe-shaped microstructure with different length-to-width ratios. As shown in Fig. 2B, the current density is not continuous and always has a higher value on one side near the electrode. By comparing the top view and section view of the current density simulation, it can be found that the microstructures with the length-to-width ratios of 1:4 and 1:6 do not have enough distance to generate the current density gradient along the long axis and only slightly decrease and then return to a high level. The 1:8 and 1:10 ratio microstructures exhibit a smooth and constant decrease along their entire length, which results in an enhanced shape-morphing ability. When the length-to-width ratio exceeds 1:12 and 1:14, the current density gradient only exists at the beginning of the microstructure and remains at 10 A/m^2 at the end part. The shape-morphing results also support these current density distribution types, and the microstructures with the length-to-width ratios of 1:4 and 1:6 exhibit slight bending, owing to the lack of the current density gradient. Optimum shape-morphing results were obtained with the 1:8 and 1:10 ratio microstructures. The

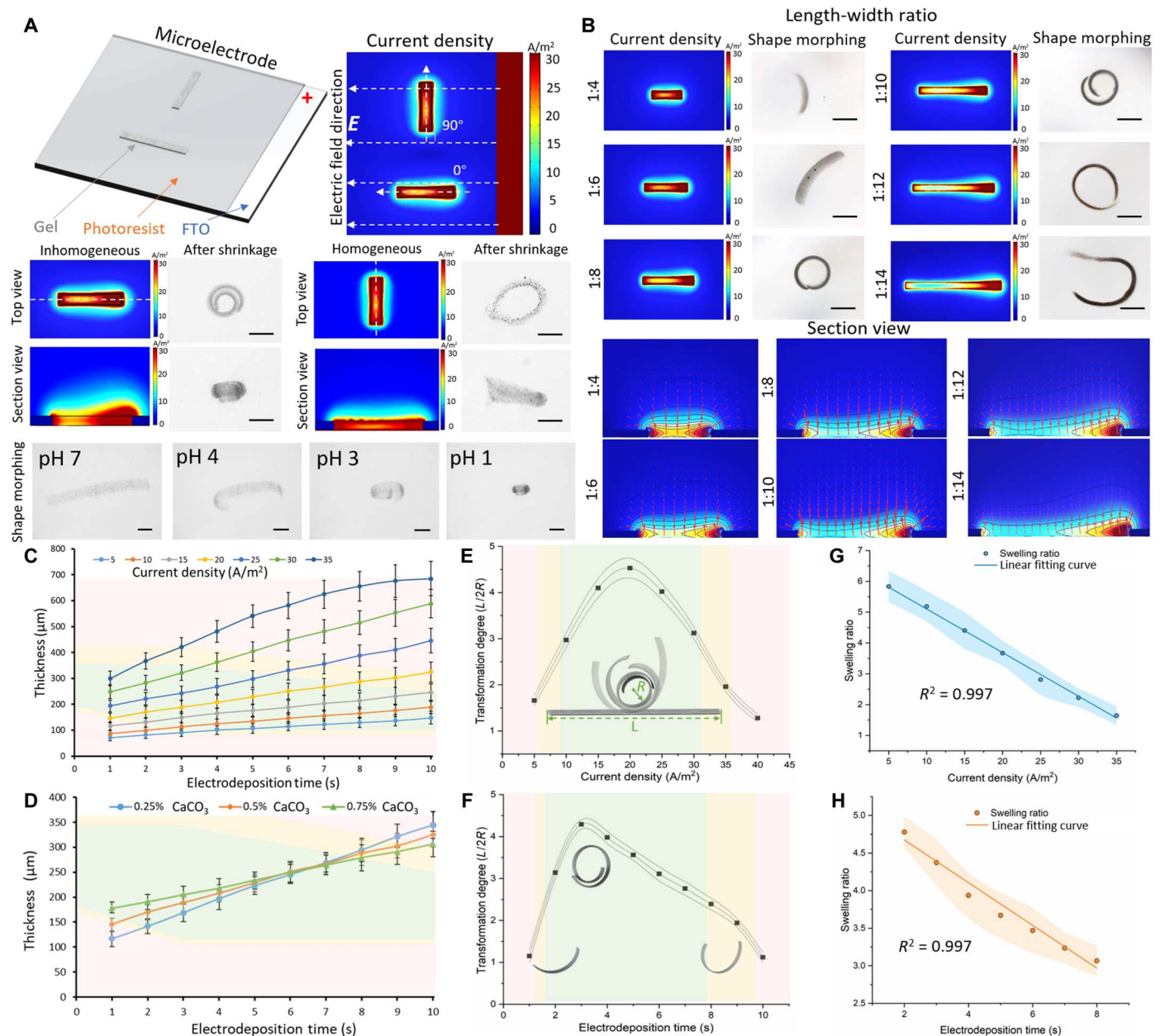


Fig. 2. Bending deformation of a stripe-shaped hydrogel microstructure. (A) Current density simulation and shape morphing of horizontally and vertically stripe-shaped hydrogel microstructures under pH response. Scale bars, 300 μm . (B) Current density simulation and shape morphing of the stripe-shaped hydrogel microstructures with various length-to-width ratio. Scale bars, 300 μm . (C) Time-dependent electrodeposition thickness as a function of current density. Each dot represents the average thickness of five different MMRs under a pH shift with stripe shapes \pm SEM. (D) Time-dependent electrodeposition thickness as function of CaCO_3 concentration. The green area indicates that the microstructures can perform shape morphing. The yellow area indicates that the microstructures can perform partial shape morphing. The red area indicates that the microstructures perform almost no shape morphing. Each dot represents the average thickness for five different MMRs under a pH shift with stripe shapes \pm SEM. (E) Transformation degree of the hydrogel microstructures with various current densities represented by the ratio between the half length of the stripe-shaped microstructure ($L/2$) and the minimum radius of curvature of the spiral microstructure (R). Each dot represents the average transformation degree of structures with stripe shapes \pm SEM with $n = 5$. (F) The transformation degree of the hydrogel microstructures with various electrodeposition durations. Each dot represents the average transformation degree of structures with stripe shapes \pm SEM with $N = 5$. (G) Swelling ratio between the volume of the stripe-shaped microstructures formed with different current densities before and after shrinkage ($V_{\text{before}}/V_{\text{after}}$). Each dot represents the average swelling ratio of structures with stripe shapes \pm SEM with $N = 5$. (H) Swelling ratio of the stripe-shaped microstructure volumes formed with different electrodeposition times before and after shrinkage ($V_{\text{before}}/V_{\text{after}}$). Each dot represents the average swelling ratio of structures with stripe shapes \pm SEM with $N = 5$.

microstructures with the length-to-width ratios of 1:12 and 1:14 exhibited less bending or partial bending.

Apart from the length-to-width ratio, the current density, electrodeposition time, and CaCO_3 concentration are also important factors influencing the shape-morphing behavior. As shown in Fig. 2C, the current density and electrodeposition time always have a positive relationship with the gel thickness. When the current density exceeds 35 A/m^2 , the electrodeposition time has a nonlinear relationship with the thickness if the electrodeposition time is longer than 7 s. When the current density exceeds 60 A/m^2 , the hydrogel structures will have no shape-morphing ability in any of the electrodeposition duration. In Fig. 2C, the green area indicates that the microstructures are able to perform shape morphing, the yellow area indicates that the microstructures are able to perform partial shape morphing, and the red area indicates that the microstructures are completely incapable of performing shape morphing. In summary, only the microstructure with a thickness of 100 to $290 \mu\text{m}$ can perform shape morphing. With a current density of 30 A/m^2 , 0.25% CaCO_3 provides less thickness within shorter electrodeposition time compared with 0.75% CaCO_3 , because the dissociative Ca^{2+} concentration is relatively lower in the 0.25% CaCO_3 hydrogel deposition solution and less Ca^{2+} can be generated within a short electrodeposition period (Fig. 2D). The 0.75% CaCO_3 hydrogel deposition solution can more easily form a thick and condensed hydrogel network within a shorter electrodeposition period, but the compact network will hinder the Ca^{2+} transformation against the thickness. Hence, compared with 0.25% CaCO_3 , if the electrodeposition time is longer, the 0.75% CaCO_3 hydrogel deposition solution would tend to form a condensed gel network instead of facilitating a thicker gel. As shown in Fig. 2E, the fabrication parameters of 0.5% CaCO_3 concentration and 5-s electrodeposition time enabled the highest degree of transformation at 20 A/m^2 with pH 1 adjusted by HCl injection according to the current density. Figure 2F shows the ratio between the half length of the stripe-shaped structure ($L/2$, before shrinkage) fabricated using 0.5% CaCO_3 concentration and current density of 20 A/m^2 and the curvature of the spiral structure (R , after shrinkage) with pH 1 adjusted by HCl injection according to the electrodeposition duration. Obviously, the electrodeposition time of 3 s provided the largest shape-morphing ability and curvature. By dividing the volume before the shrinkage by the volume after the shrinkage, it can be found that the swelling ratio ($V_{\text{before}}/V_{\text{after}}$) significantly decreased from 5.8 to 1.6 as the current density increased (electrodeposition time, 5 s) in Fig. 2G. However, when the electrodeposition time changed (current density, 20 A/m^2), the volumes exhibited a similar trend before and after the shrinkage, and the swelling ratio only decreased from 4.7 to 3.0 as shown in Fig. 2H.

Helical microstructure fabrication through unidirectional electric fields

To program the shape morphing of the hydrogel microstructure, changing the angle between the microstructure and the electric field is a possible option for controlling the current density distribution in the 3D hydrogel network. Therefore, the angles 22.5° , 45° , -45° , and 67.5° were selected as examples to demonstrate the unparallel electric field effect on the current density distribution and stripe microstructure deformation as illustrated in Fig. 3. Figure 3A shows the microelectrode setup and simulation results for the current density distributions. As can be seen, the current density

gradient is still generated along the electric field direction. Because the stripe-shaped structures include an angle (θ) between the electric field and the long axis, a gradient also exists on the short axis. In Fig. 3B, the top view shows that the current density gradient in the short axis changes with the angle between the microstructure and the electric field direction. On the basis of the experimental results, the microstructure always deforms into a helical structure, which indicates that torque does not only exist on the long axis but also exist on the short axis (see movie S3). Moreover, the helical structure becomes longer and looser as the angle increases. Figure 3C shows the relationship between the angle and the parameter of the helical microstructures. As the angle increases, the diameter of the helical structure decreases from a curling (0°) to a coil structure, and the length eventually becomes larger than that of the straight structure (90°). The stress simulation also revealed that the strain on the short axis increases with the angle between the electric field and the stripe microstructure, which means that the current density gradient determines the strain and stress of microstructure shape morphing. As the angle between the structure and the electric field increases, the microstructure exhibits less shear strain along the short axis.

To predict the shape morphing generated by the unidirectional electric field, we measured the geometries after shrinkage and normalized those into helical microstructures, which were further simplified into helical lines. By drawing the projection of these helical lines, the curved structure of each helical microstructure was obtained as a function of $y = A \times \sin Bx$, as shown in Fig. 3D. When the microstructure was aligned with an angle of 45° between the electric field, the electrodeposition time and CaCO_3 concentration also affected the geometry of the helical structure. Figure 3E shows that, with both 0.5% CaCO_3 and 0.75% CaCO_3 , the helical structure became longer from 3 to 5 s and wider from 5 to 7 s. CaCO_3 microstructures (0.25%) kept becoming wider and shorter from 3 to 7 s. As shown in Fig. 3F, with constant 0.5% CaCO_3 , the microstructure fabricated with the higher electrodeposition time always had a shorter length and a larger diameter. On the basis of the simulation results and the helical line, the curve fitting tool of MATLAB was used to express A and B as a function of the current density (c) and electrodeposition time (t) with constant 45° and 0.5% CaCO_3 concentration, as expressed by

$$A = 0.08t^2 - 0.3t + 5.54 - 0.84 \cos 1.26c - 0.23 \sin 1.26c \quad (1)$$

$$B = 0.04t^2 - 0.17t + 7.33 - 0.75 \cos 0.21c - 0.01 \sin 0.21c \quad (2)$$

Because this function has a limited application range, we used FEA to help design the gel structures to achieve the desired 3D shape morphing.

Bidirectional and circular electric fields for shape morphing

In addition to the unidirectional electric field, various types of bidirectional and circular electric fields can be induced to provide more shape-morphing capabilities to the hydrogel microstructures. This study conducted FEA based on the deformation gradients to reproduce the shape transformations. As shown in Fig. 4A, stripe-shaped microelectrodes were placed at the middle of the photoresist. The microstructure parallel to the electric field only performed bidirectional shape morphing and transformed into a heart-shaped microstructure as shown in movie S4. However, if the

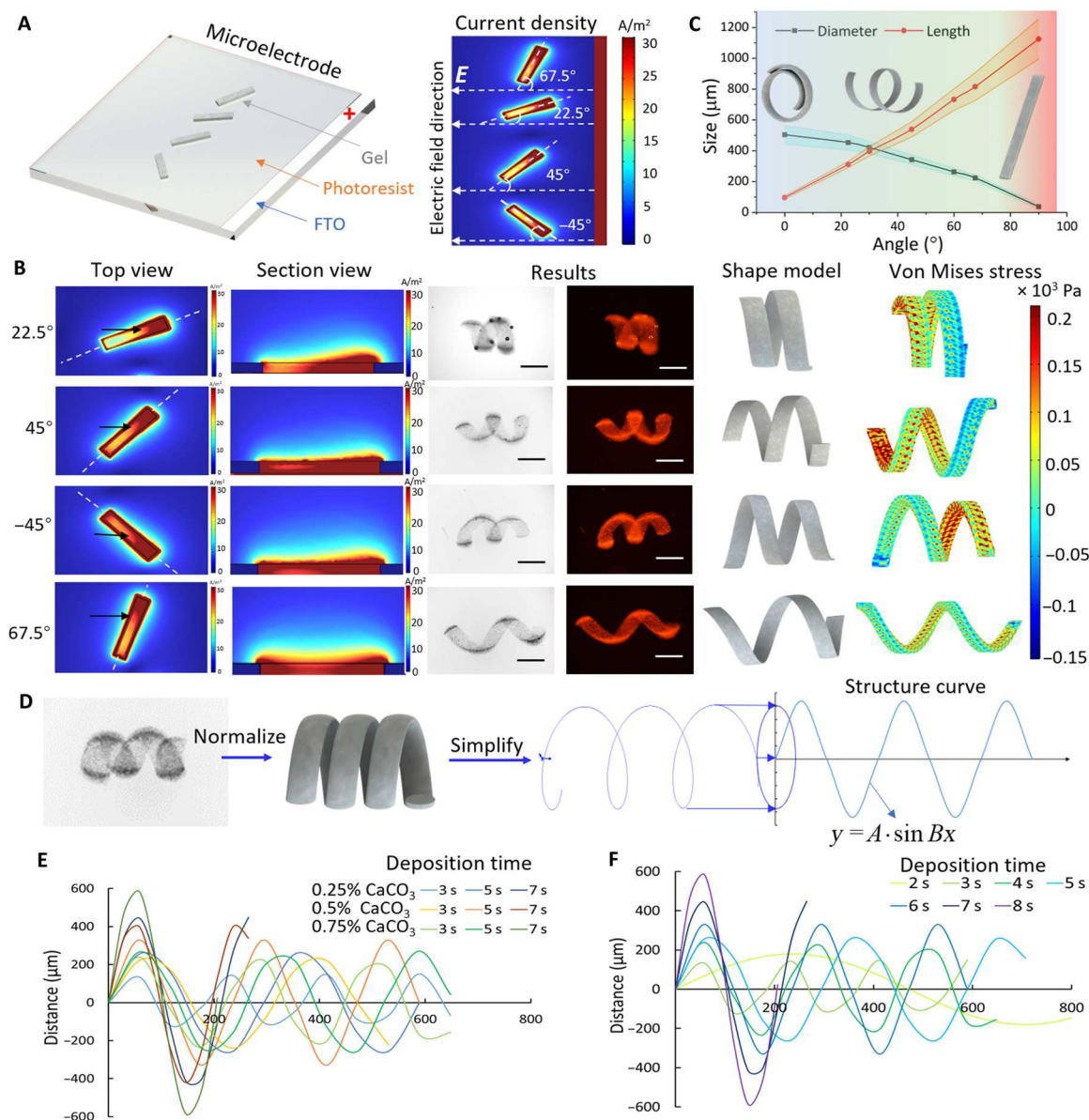


Fig. 3. Unidirectional shape morphing. (A) Pattern of the microelectrode design and current density simulation of different microelectrodes with various angles along the unidirectional electric field (E); the white dashed lines represent the electric field direction. (B) Current density simulations of rectangular-shaped microelectrode with various directions along the electric field. The white dashed lines represent the position of the section view of the microelectrode. The black arrows indicate the position with a significant current density difference. The fluorescent and bright-field images show the helical microstructures after shrinkage with pH 1. Scale bars, 300 μm . On the basis of the 3D shape modeling, the simulation illustrates the structural stress in the helical microstructures. (C) The direction of the electric field affects the geometry of the helical structure after shape morphing. Each color band indicates \pm SEM with $N = 5$ for the microstructure dimension. (D) Process of quantifying the results of shape morphing from the experimental helical structures to the simplified and normalized structure curve. (E) Helical microstructure curve-dependent distance as function of CaCO_3 concentration varying from 0.25 to 0.75% with electrodeposition duration of 3, 5, and 7 s. (F) 0.5% CaCO_3 helical microstructure curve with different electrodeposition durations from 2 to 8 s.

microstructure had a 45° angle between the electric fields, then the two ends of the microstructure will shift between each other and will not meet at the middle point, instead of bending and meeting at the middle point. When the stripe structures were replaced by cross structures, the cross structures yielded similar results. When the cross microstructure was placed in an X shape along the electric field, the microstructure bent to the centrosymmetric line of the structure and electric field. When the cross microstructure was

placed into a positive sign (+) shape along the electric field, the microstructure bent to the central point of the structure as shown in Fig. 4B and movie S5. However, when the microelectrode was changed from a bidirectional to a circular electric field, an endocentric electric field was induced in the circular microelectrode, and there was no directional difference between each cross structure. Thus, both cross microstructures bent toward the central point as illustrated in Fig. 4C.

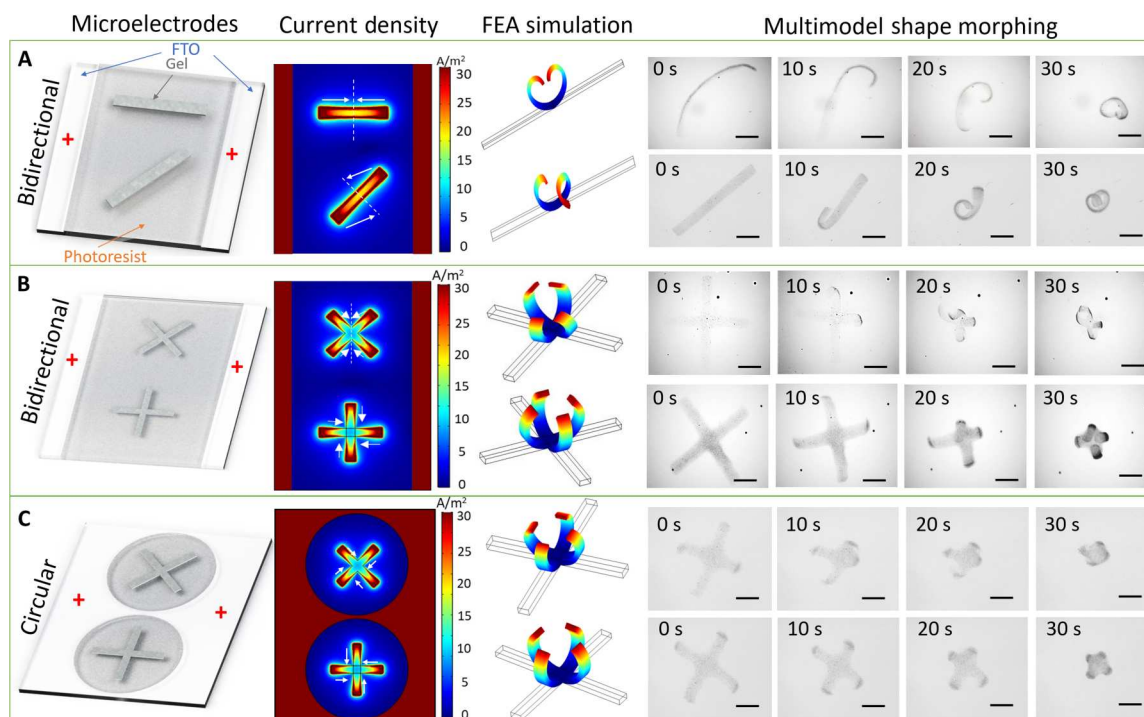


Fig. 4. Different shape-morphing behaviors under bidirectional and circular electric fields. (A) Stripe-shaped microstructures exhibiting shape morphing at the angles of 0° and 45° along the bidirectional electric field. With different orientations, the horizontal stripe microstructure morphed into a heart shape through bidirectional bending, and the diagonal stripe microstructure transformed into a helical structure. Scale bars, $500\ \mu\text{m}$. (B) The cross-shaped microstructures placed into "X" and "+" shapes along the bidirectional electric field resulted in different shape morphing. The X-shaped directional microstructure performed axial-symmetrical shape morphing, while the + directional microstructure performed central-symmetrical transformation. Scale bars, $500\ \mu\text{m}$. (C) The cross-shaped microstructures in the circular electric field only exhibited central-symmetrical deformation and were not influenced by the orientation. Scale bars, $500\ \mu\text{m}$.

Multicomponent and multitransformation through modularized fabrication

According to the design of various electric fields, hydrogel microstructures can be endowed with arbitrarily shaped morphing models. To develop a single multitasking microrobot, we separately deposited alginate droplets onto the different parts of the microelectrode with customized components. Thus, a multicomponent system was embedded into a single microstructure. As shown in Fig. 5A, three separated droplets were placed on different parts of the microstructure. After the electrodeposition, the microstructures could still perform different types of shape morphing. In addition to endowing the microrobot with a multicomponent system, different shape transformations can also be programmed into different microrobot modules. As shown in Fig. 5B, the T-shaped microstructure provides bidirectional bending in the horizontal part and unidirectional twisting in the vertical part. Moreover, these modules can be separately loaded with green and red fluorescent nanoparticles or cells and magnetic nanoparticles (MNPs). On the basis of this modularized fabrication method, two-, three-, and four-fingered microrobots were loaded with MNPs in the vertical part as the head of the microrobot to provide propulsion, as shown in Fig. 5C and movies S6 to S8. The tail part is customizable and can be loaded with cells, drugs, and visualization agents without influencing the actuation module loaded with MNPs. Microrobots with different finger shapes for grasping arbitrary objects were designed with different geometries and profiles.

Magnetically actuated, multimodal, soft-bodied microrobotic locomotion

After loading the drugs, contrast agents, cells, and MNPs into the different hydrogel microstructure modules, the microstructures can be considered as MMRs with two types of locomotion modes: fish-like and caterpillar-like locomotions. To achieve fish-like undulatory swimming, we embedded MNPs into the vertical module of the two-fingered MMRs as the head of the microrobot and magnetized MNPs along the long axis. On the basis of the oscillating field (B_o) along the X-Y plane, the MMRs could turn by 45° and be perpendicular to the Z plane. The propulsion direction was controlled through the uniform field strength (B_u) and oscillating field strength (B_o) as shown in Fig. 6A. Figure 6B and movie S9 show the swimming trajectories of the MMR with a "B," "I," and "T" shape under electromagnetic system control (frequency, 4 Hz). Figure 6C shows the different postures in cyclic swimming. With different B_o frequencies, the MMR exhibited different morphologies as the endpoint pendulum angle of the magnetic module as illustrated in Fig. 6D. The pendulum angle represents the angle between the moving direction and the MMR direction. As the frequency increased, the MMR had a smaller pendulum angle and a higher oscillating velocity (ω). The higher concentration of MNPs always provided a higher step-out frequency, and the propulsion speed reached $8.3\ \text{mm/s}$ as shown in Fig. 6E. When the oscillating field direction was changed from the X-Y plane to the X-Z or Y-Z plane, the four-fingered MMR could perform caterpillar-like motion as shown in Fig. 6 (F and G) and movie S10. In the

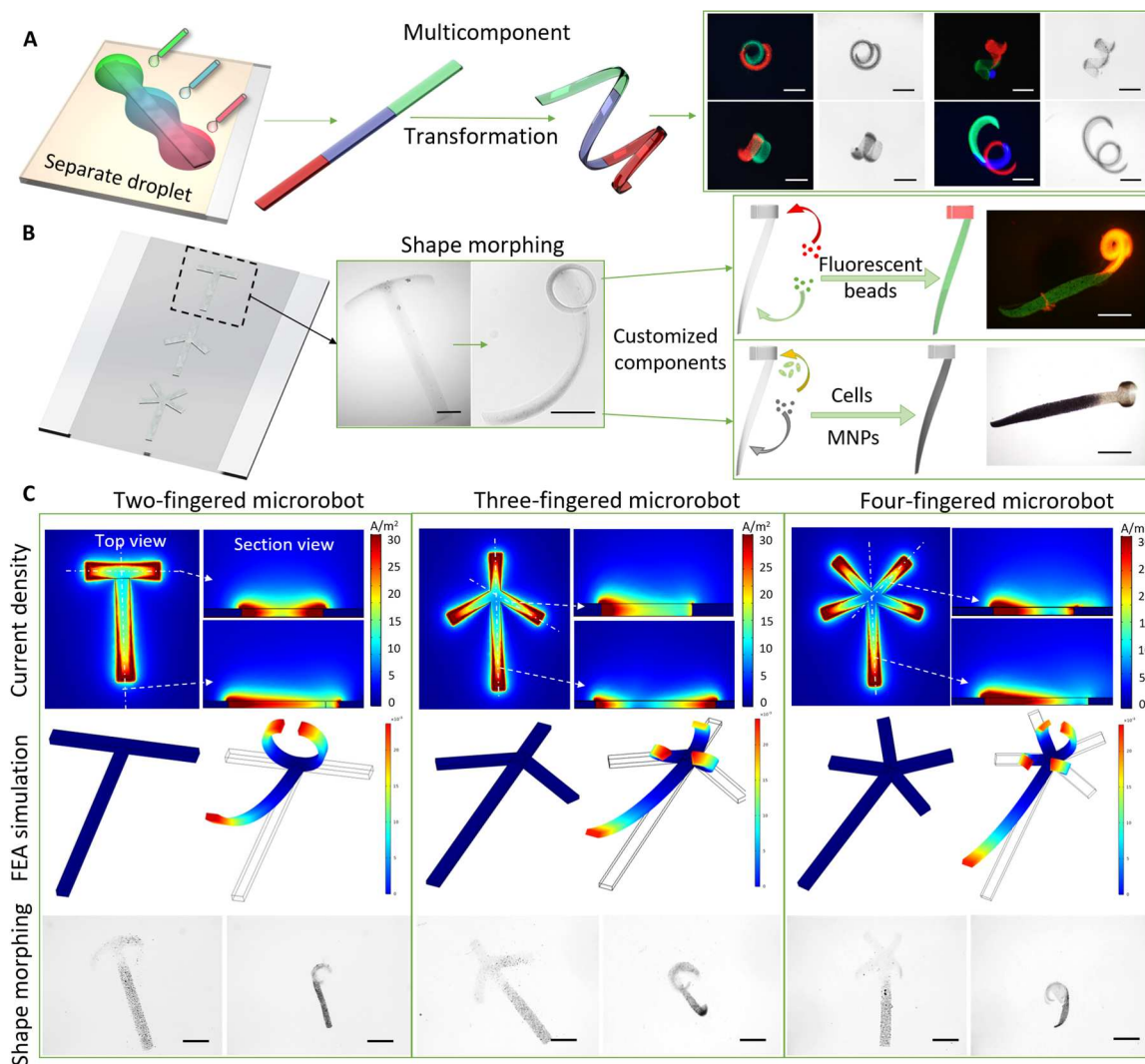


Fig. 5. Fabrication of modular multicomponent soft microrobots with multiple transformations. (A) Stripe-shaped microstructures fabricated by applying droplets with fluorescent green, red, and blue nanoparticles to different parts of the microelectrode. After the shape transformation under pH or ionic stimuli, the stripe microstructure transformed into helical and coiled microstructures with two and three separated modules. Scale bars, 500 μm . (B) Modularized fabrication of two-fingered microrobot with customized components including fluorescent nanoparticles, cells, and MNPs and execution of bidirectional bending on horizontal module and twisting on vertical module. Scale bars, 500 μm . (C) The two-, three-, and four-fingered microrobots with modular design can respond to ionic and pH stimuli. The white dashed line indicates the position of the section view of the current density simulation results. The FEA simulation revealed the shape-morphing process of the two-, three-, and four-fingered microrobots. Scale bars, 600 μm .

caterpillar-like undulatory motion, there are two typical postures: upward and downward. The oscillating field (B_o) kept undulating the magnetic module and transferred the motion to the nonmagnetic module. Thus, propulsion similar to that of fish-like motion was generated. As the frequency and strength of B_o increased, the velocity of MMR increased and the step-out frequency was 3 Hz, as shown in Fig. 6H. By applying a uniform field (B_u) along the Z axis, the MMR could stand up and perform pitching motion by changing the B_u direction. On the basis of these motion series, the MMR could carry MNPs and fluorescent nanoparticles to precisely move, grasp, disassemble, and release the payload to the spherical target as shown in Fig. 6J and movie S11.

In vitro cell delivery through physical contact

Because of the soft-bodied microrobotic locomotion, the MMR could be an ideal cell delivery system because cells and MNPs can be loaded onto different MMR modules. In the two-fingered MMR, the horizontal module was loaded with green fluorescent protein (GFP)-enhanced human umbilical vein endothelial cells (HUVECs), and the vertical module was loaded with MNPs. The MMR could swim to the target tubular area and self-grasp onto it in response to pH or ionic stimuli. After 5 days of cell culture, 2.7×10^4 HUVECs migrated to the target area, which means that the MMR completed the cell delivery task, and the magnetic module could be removed from the microrobot by changing the pH or ionic strength. During this process, the magnetic module could be easily dragged out of the MMR by the outer magnetic

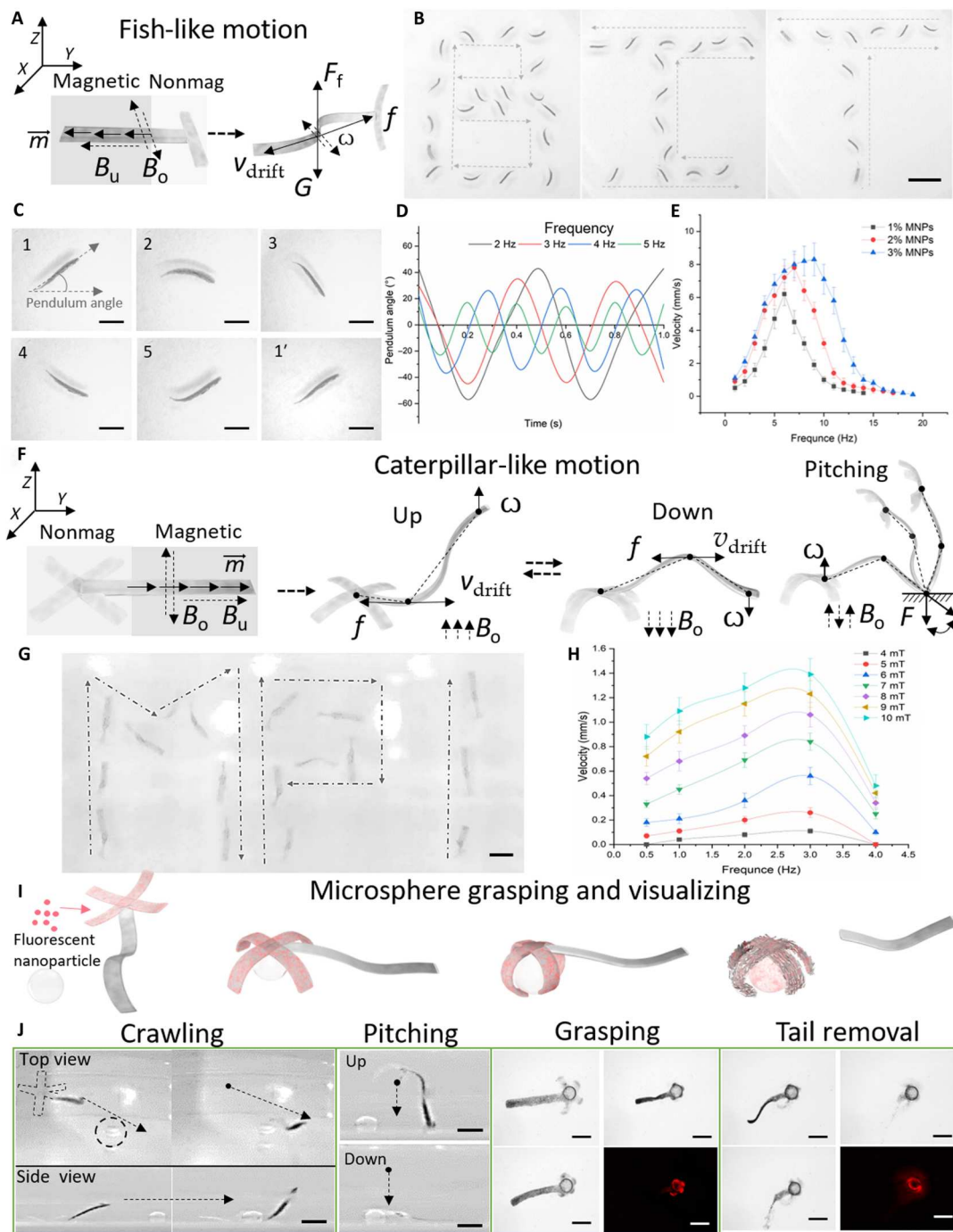


Fig. 6. Fish- and caterpillar-inspired locomotion modes. (A) Schematic illustration of magnetic actuation of the fish-like locomotion under an oscillating field (B_o) and a uniform field (B_u), where \vec{m} is the magnetic torque, V is the two-fingered MMR velocity, f is the friction force, ω is the oscillating velocity of the microsphere, and F_f is the floating force generated by the swimming of the MMR. (B) Swimming trajectory of MMR with “B,” “I,” and “T” shape. Scale bars, 3 mm. (C) Posture of MMR at different time points. Scale bars, 1 mm. (D) Pendulum angle of MMR at frequency. (E) Velocity–frequency profiles for MMRs with different MNP concentrations based on fish-like motion. Each dot represents the average velocity of three different MMRs with two-fingered shapes \pm SEM. (F) Illustration of caterpillar-like locomotion of four-fingered MMR containing magnetic and nonmagnetic modules; B_o and B_u represent the oscillating and uniform magnetic fields, respectively, V is the four-fingered MMR velocity, \vec{m} is the magnetization torque of the MMR, f is the friction force, ω is the oscillating velocity, and F is the holding force. (G) Crawling trajectory of MMR with “M,” “P,” and “I” shape. Scale bar, 1 mm. (H) Velocity–frequency profiles for MMRs with different magnetic oscillating fields (B_o) (4 to 10 mT) based on caterpillar-like locomotion. Each dot represents the average velocity of three different MMRs with four-fingered shapes \pm SEM. (I) Illustration of microspheres grasping, visualization, and corresponding transformations of fluorescent nanobead–loaded MMR under ionic stimulation. (J) Fluorescent nanobead–loaded four-fingered MMR crawling toward microspheres, placing head (nonmagnetic) part onto the microspheres using a pitching motion, grasping the microspheres upon application of CaCl_2 solution, self-releasing the magnetic microspheres upon the application of sodium citrate solution followed by full dissolution, and visualizing the microspheres by fluorescent microscopy. Scale bars, 1 mm.

field, which largely ensured the biosafety of MNPs. Figure S2 shows the biocompatibility comparison results for commonly used MNPs and the modular MMR. On the basis of the results, these commonly used magnetic particles cannot mix with the cells for long-term culture. Moreover, we can remove the magnetic module out of the organism, such as toward the colon for defecation, by magnetic control after the separating process, which makes it even safer. Thus, the MMR protects the functional payload from the magnetic or chemical propulsion module compared with a microrobot with a uniform composition. After the MMR was removed, the delivered HUVECs kept proliferating and fully covered the target area as shown in Fig. 7 (A to C) and movie S12.

Ex vivo contrast agent delivery

Apart from cell delivery, the MMR can also deliver a contrast agent, such as microbubbles and fluorescent nanoparticles, onto a target area to achieve local visualization as shown in Fig. 8. The intestine of a Sprague-Dawley rat was extracted and immersed into an artificial stomach liquid. Fluorescent nanoparticles and microbubbles were embedded into the cross-module of the MMR, and the MNPs were loaded in the beam module to provide propulsion. The MMR moved with caterpillar-like locomotion. The ultrasound images (Fig. 8A) show that the MMR was initially located at the left end of the intestine at the time of 30 s. Under the magnetic field, the MMR moved along the intestine (see movie S13). In the future clinical applications, the MMR can also be embedded with other

contrast agents for tracking the 3D locomotion through a clinical imaging system. Besides, the viscosity of the liquid environment in the gastrointestinal tract can be tuned by abrosia, diarrhea (for bowel preparation), and water drinking. Because of the loaded fluorescent nanoparticles, the MMR could be visualized by fluorescent microscopy as shown in Fig. 8B and movie S14. After the MMR arrived to the target area, the MMR dissolved within 3 min after injecting the artificial intestine liquid. The dissolving time under different injection rates was measured as shown in fig. S3.

DISCUSSION

To endow a soft microrobot with more functionality, this study developed a modularized aniso-electrodeposition method to fabricate an environmentally adaptive MMR (size range, 500 to 3 mm after shrinkage). The MMR has various shape-morphing abilities, and various compositions can be embedded into different parts of the MMR. By controlling the electric field pattern, the 3D microstructure can be endowed with a 3D shape-morphing ability. The strain and stress of shape morphing are mainly determined by the thickness, electrodeposition time, and current density distribution and gradient. A lower current density corresponds to a lower cross-link degree and a larger swelling ratio after shrinkage. However, a larger current density gradient improves the self-shape-morphing ability of the hydrogel microstructures. Hence, by controlling the microelectrode shape, applied electric field direction, and current

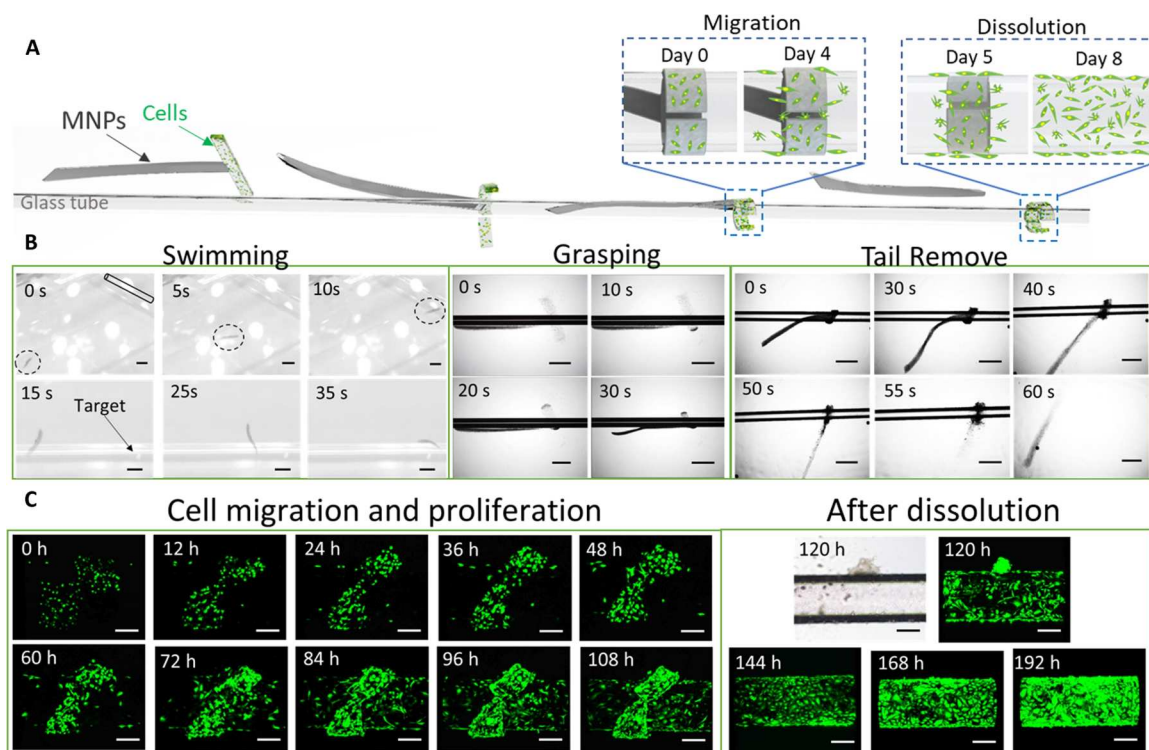


Fig. 7. Soft microrobotic cell delivery demonstration through physical contact. (A) The MMR is moved to the target area, attached to the structure, grasped the target through the functional module, delivered the cells, and removed the propulsion module through magnetic control and transformation under ionic stimulation. (B) Optical images showing the MMR propulsion, self-trapping of the tubular target area, and removal of the magnetic module after the cell delivery was completed. Scale bars, 1 mm. (C) Fluorescent optical microscopic images of GFP-enhanced HUVEC proliferation and migration after the MMR grasped the target area; the delivered cells fully covered the target area after the removal of the propulsion module. Scale bars, 200 μ m.

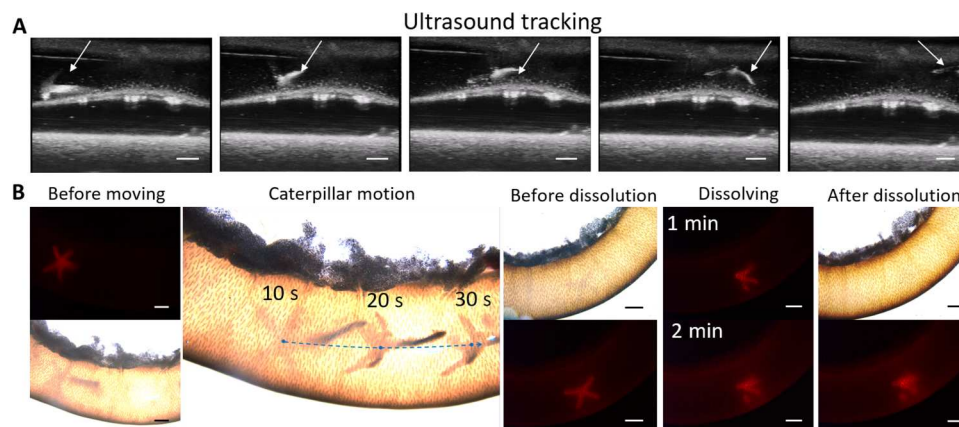


Fig. 8. Ex vivo magnetic locomotion of the MMR inside the small intestine and delivery of a contrast agent. (A) Ultrasound images for tracking the MMR locomotion under magnetic control. Scale bars, 1 mm. (B) Ex vivo propulsion and target delivery of MMR carrying MNP contrast agent and fluorescent microbeads and controlled by external magnetic field. Scale bars, 1 mm.

density distribution, different types of 3D shape morphing can be programmed into the simplest microstructures. Considering the simplest stripe shape as an example, stripe microstructures fabricated using different electric fields can transform into spiral-, helical-, heart-, and Möbius ring-shaped structures in response to pH or ionic stimuli. Moreover, the chirality, screw pitch, and length of the helical microstructures can be accurately programmed. For more complex structures, the form and axis of self-deformation can also be controlled, and a single microstructure can be endowed with the ability to morph into different shapes. To endow the MMR with multitasking capability, different compositions can be loaded into different MMR modules to perform different functions within the integrated microrobot without mutual interference. With the same modular design concept as conventional robotic systems, MNPs can be embedded into the MMR as a propulsion module, and cells, contrast agents, and drugs can be loaded onto another part of the MMR functioning as a task module. In different tasks, the loading can be customized, and at least three different compositions can be loaded onto the MMR through a single-step process.

By embedding the MNPs into the microstructure, the MMR can perform fish-like and caterpillar-like locomotions according to the situation at hand. The fish-like locomotion is more effective and faster than caterpillar-like locomotion, which is more suitable to long-distance locomotion. After the MMR arrives near the target, it can transition to caterpillar-like locomotion to precisely grasp the target through pitching. In addition to MNPs, different MMR regions can be used as functional modules carrying cells, contrast agents, and fluorescent nanoparticles. Thus, mutual interference between the propulsion module and biofunction modules can be prevented. Moreover, to protect the local environment from MNPs, the propulsion module can be partially removed after fulfilling the biomedical task. This modular design significantly reduces limitations in the selection of the biofunctional object and propulsion component.

In *in vitro* and *ex vivo* tests, the MMR already achieved propulsion, target grasping, cell migration, proliferation, and propulsion module removal. On the basis of cell delivery through physical contact, the MMR can more precisely and locally deliver a

payload to a target area instead of spreading the payload. The modular design protects the functional payload from the magnetic or chemical propulsion module, which eliminates restrictions regarding the propulsion component and provides a safer and more stable microenvironment for the payload. Therefore, the proposed delivery system could be used in future targeted immune cell and drug delivery and precise tumor treatment applications.

Through the aniso-electrodeposition method, an electric field can program various shape-morphing types into the same microstructure. The proposed modular design allows customizable, single-step, and high-throughput fabrication along with functional components for the integration of versatile locomotion and transformation patterns, including propulsion, targeting, pH- and ionic-responsive grasping, payload delivery, and payload release. The proposed fabrication and design approach provides the groundwork for developing the next generation of soft microrobots for controlled propulsion and cargo delivery in the gastrointestinal tract.

MATERIALS AND METHODS

Production of microelectrodes

The detailed design of the microelectrodes was developed as shown in fig. S4 to conduct electrodeposition. Through spin coating, a 10- μm photoresist (AZ5214) layer was first applied to the surface of a 50- μm -thick fluorine-doped tin oxide (FTO) glass (Huanan Xiangcheng Inc., Shenzhen, China). The photoresist-coated FTO glass was then baked for 1 min at 100°C on a hotplate. Subsequently, the photoresist-coated FTO glass was exposed to a homogeneous ultraviolet light through a predesigned photomask. Then, the FTO glass was developed for 45 s in an AZ developer, yielding 10- μm -thick patterns. Last, the patterned FTO glass was heated on a hotplate for 2 min at 120°C to fix the photoresist. The anode plate is an FTO plate coated with patterned photoresist as microelectrodes, which connect to the positive electrode of the power supply. In addition, the cathode is a pure FTO plate connected to the negative electrode of the power supply. There are two 2-mm spacers between the cathode and anode.

Fabrication of MMRs

The alginate microstructures are created by mixing the hydrogel deposition solution that contained 1% (w/v) sodium alginate and 0.25, 0.5, or 0.75% (w/v) CaCO₃ particles. Before electrodeposition, the hydrogel deposition solution was combined with 1, 2, or 3% (w/v) MNPs, 2% (v/v) fluorescent nanobeads and cells to fabricate different modules of the MMRs. The MNPs (Ni nanoparticles) were purchased from Beijing Zhongkeleiming Technology Co. Ltd. (Beijing, China). First, a 2-ml hydrogel deposition solution was dropped on the anode plate and then placed the cathode plate on the top of the anode as shown in the fig. S1. Second, a direct current voltage of 2 to 6 V was applied on the FTO layers of both anode and cathode plates for 1 to 10 s. Before detaching the hydrogel microstructures, the anode plate was placed on a vibrating sample magnetometer (EZ7, Microsense, USA) to magnetize the MMRs. The MMR (still on the anode plate) was magnetized along its horizontal direction with external magnetic strength (1.0 T) to develop remanence in the directional arrangement of the nickel nanoparticles so as to maximize the magnetic moment and driving force. Then, the anode plate was rinsed with Hepes buffer in a 10-cm-diameter petri dish for more than 3 min after the electrodeposition process until the calcium alginate hydrogel microstructures were fully detached from the anode plate. When the Ca alginate microstructures had been fully detached, the alginate microstructures were transferred to a 6-cm-diameter petri dish containing Hepes buffer. Then, CaCl₂ solution (1.1%, w/v) and sodium citrate solution (1%, w/v) were slowly injected until the microstructures were fully transformed. Photographic images were captured by a Leica M205 microscope under a bright field. Last, the MMR volume was measured by scanning the entire structure under a confocal microscope (A1, Nikon, Japan).

Magnetic control system

The coil setup generated a uniform magnetic field with a maximum strength of 11 mT within a workspace with the size of 4 cm by 4 cm by 4 cm. The magnetic field was controlled by modulating the currents in the electromagnetic coils using six independent motor driver units (SyRen25) and an Arduino microcontroller operating at 1.2 kHz. The robot's motion was tracked using two cameras (aCa2040-90uc, Basler). The first camera operated at 120 frames/s (fps) with a frame size of 2040 by 1020 pixels and was placed orthogonal to the Y-Z plane of the workspace to observe the robot from the side. The second camera operated at 60 fps with a frame size of 2040 by 1400 pixels and had a top view of the workspace through a mirror placed at an angle of 45° above the test surface.

In vitro tests

The GFP-enhanced HUVECs were obtained from the School of Life Science and Technology of Beijing Institute of Technology. The HUVECs were cultured in Dulbecco's modified Eagle's medium with phenol red, 10% fetal bovine serum, and 1% penicillin and streptomycin (Gibco, Carlsbad, CA, USA). The LIVE/DEAD assay was conducted by calcein acetoxymethyl ester and propidium iodide (Dojindo Molecular Technologies Inc., Kumamoto, Japan) fluorescein staining. The pH of culture medium was tuned to 6.0 to 6.5 for 1 to 2 min to soften the MMRs and separated the magnetic module sequentially. The MMR locomotion was controlled by an external magnetic system, as mentioned above. Before the in vitro test, the glass tube was coated with a layer of poly-lysine and

collagen (Gibco, Carlsbad, CA, USA). The cell proliferation process was observed by scanning the entire structure under a confocal microscope in a living cell workstation (A1, Nikon, Japan).

Ex vivo tests

The intestines were obtained from Sprague-Dawley rats received from the Institute for Animal Welfare, Veterinary Service, and Laboratory Animal Science (Einrichtung für Tierschutz, Tierärztlichen Dienst, und Labortierkunde), Eberhard Karls University, Tuebingen, Germany. The animals were kept under standardized and sterile conditions (room temperature of 20° ± 1°C, relative humidity of 50 ± 10%, 12-hour light/12-hour dark cycle) and received food and water ad libitum. The rats were euthanized, the abdominal cavity was opened, and the small and large intestines were removed from the stomach. The MMR loaded with fluorescent microbeads (Polysciences Inc., USA; red color, diameter of 1 μm), contrast agent (Vevo MicroMarker Non-Targeted Contrast Agent, Fujifilm Visualsonics Inc., Canada), and MNPs was injected into the intestine. The intestine was filled with artificial stomach liquid (Solarbio, Beijing, China), and the ends of the intestine were then sealed using two plastic clips. The MMR was manipulated using a magnetic system. After the MMR moved to the middle part of the intestine, artificial intestinal liquid (Solarbio, Beijing, China) was injected near the MMR's position using a syringe pump. The manipulation process was observed using a Vevo 3100 imaging system (Fujifilm Visualsonics Inc., Canada) combined with a Leica M205 microscope under a bright and fluorescent field with an excitation of 510 nm and an emission of 600 nm.

Finite element analysis

FEA was conducted using commercial software (COMSOL, version 5.6, COMSOL Inc.). To understand the transformation behavior of the investigated structures, a nonlinear elastic material was used to simulate the nonlinear responses of the aniso-deposited microstructures to changes in the environmental pH. The 3D current density distribution (C) is calculated by

$$C = \sigma E \quad (3)$$

where σ represents the electroconductivity and E is the electric field strength. The swelling ratio (λ_0) is related to the current density (C_0) as measured in Fig. 2G, and the data are fitted in the curve as shown in Eq. 4 ($R^2 = 0.997$). Equation 4 is applicable to a current density from 5 to 40 A/m², where the alginate hydrogel can be normally electrodeposited. Relative to the retractile network, the network in this state swells with isotropic stretches. We denote this free-swelling stretch by λ_0 and the deformation gradient by \mathbf{F}_0 as

$$\lambda_0 = -0.14C_0 + 6.5 \quad (4)$$

$$\mathbf{F}_0 = \begin{pmatrix} \lambda_0 & 0 & 0 \\ 0 & \lambda_0 & 0 \\ 0 & 0 & \lambda_0 \end{pmatrix} \quad (5)$$

A 3D model was established and meshed using a superfine element type, and numerical analysis was carried out. The transformation of the 3D model included a nonlinear transformation analysis using the Newton's method. Similarly, FEA was carried out to design the morphological changes in other microstructures before

aniso-electrodeposition, and the detailed model design and parameters were shown in fig. S5.

Supplementary Materials

This PDF file includes:

Figs. S1 to S5

Other Supplementary Material for this manuscript includes the following:

Movies S1 to S14

[View/request a protocol for this paper from Bio-protocol.](#)

REFERENCES AND NOTES

- D. Rus, M. T. Tolley, Design, fabrication and control of soft robots. *Nature* **521**, 467–475 (2015).
- M. R. Nowicki, D. Belter, A. Kostusiak, P. Cížek, J. Faigl, P. Skrzypczyński, An experimental study on feature-based SLAM for multi-legged robots with RGB-D sensors. *Ind. Rob.* **44**, 428–441 (2017).
- S. Saeedvand, M. Jafari, H. S. Aghdasi, J. Baltes, A comprehensive survey on humanoid robot development. *Knowl. Eng. Rev.* **34**, e20 (2019).
- K. Otto, K. Hölttä-Otto, T. W. Simpson, D. Krause, S. Ripperda, S. Ki Moon, Global views on modular design research: Linking alternative methods to support modular product family concept development. *J. Mech. Des.* **138**, 071101 (2016).
- F. Soto, E. Karshalev, F. Zhang, B. E. F. de Avila, A. Nourhani, J. Wang, Smart Materials for Microrobots. *Chem. Rev.* **122**, 5365–5403 (2022).
- W. Hu, G. Z. Lum, M. Mastrangeli, M. Sitti, Small-scale soft-bodied robot with multimodal locomotion. *Nature* **554**, 81–85 (2018).
- M. Sitti, Physical intelligence as a new paradigm. *Extreme Mech. Lett.* **46**, 101340 (2021).
- M. Medina-Sánchez, V. Magdanz, M. Guix, V. M. Fomin, O. G. Schmidt, Swimming microrobots: Soft, reconfigurable, and smart. *Adv. Funct. Mater.* **28**, 1707228 (2018).
- M. Li, X. Wang, B. Dong, M. Sitti, In-air fast response and high speed jumping and rolling of a light-driven hydrogel actuator. *Nat. Commun.* **11**, 1–10 (2020).
- D. Han, Z. Lu, S. A. Chester, H. Lee, Micro 3D printing of a temperature-responsive hydrogel using projection micro-stereolithography. *Sci. Rep.* **8**, 1963 (2018).
- Y. Cheng, K. Ren, D. Yang, J. Wei, Bilayer-type fluorescence hydrogels with intelligent response serve as temperature/pH driven soft actuators. *Sens. Actuators B: Chem.* **255**, 3117–3126 (2018).
- Q. Lin, M. Tang, C. Ke, Thermo-responsive 3D-printed polyrotaxane monolith. *Polym. Chem.* **11**, 304–308 (2020).
- I. Rehor, C. Maslen, P. G. Moerman, B. G. Van Ravensteyn, R. Van Alst, J. Groenewold, H. B. Eral, W. K. Kegel, Photoresponsive hydrogel microcrawlers exploit friction hysteresis to crawl by reciprocal actuation. *Soft Robot.* **8**, 10–18 (2021).
- Z. J. Wang, C. Y. Li, X. Y. Zhao, Z. L. Wu, Q. Zheng, Thermo- and photo-responsive composite hydrogels with programmed deformations. *J. Mater. Chem. B* **7**, 1674–1678 (2019).
- H. Kim, J. H. Kang, Y. Zhou, A. S. Kuenstler, Y. Kim, C. Chen, T. Emrick, R. C. Hayward, Light-driven shape morphing, assembly, and motion of nanocomposite gel surfers. *Adv. Mater.* **31**, e1900932 (2019).
- Z. J. Wang, C. Y. Li, X. Y. Zhao, Z. L. Wu, Q. Zheng, Thermo- and photo-responsive composite hydrogels with programmed deformations. *J. Mater. Chem. B* **7**, 1674–1678 (2019).
- Z. Zheng, H. Wang, L. Dong, Q. Shi, J. Li, T. Sun, Q. Huang, T. Fukuda, Ionic shape-morphing microrobotic end-effectors for environmentally adaptive targeting, releasing, and sampling. *Nat. Commun.* **12**, 411 (2021).
- D. Jin, Q. Chen, T.-Y. Huang, J. Huang, L. Zhang, H. Duan, Four-dimensional direct laser writing of reconfigurable compound micromachines. *Mater. Today* **32**, 19–25 (2020).
- H. Li, G. Go, S. Y. Ko, J.-O. Park, S. Park, Magnetic actuated pH-responsive hydrogel-based soft micro-robot for targeted drug delivery. *Smart Mater. Struct.* **25**, 027001 (2016).
- X. Yang, W. Shang, H. Lu, Y. Liu, L. Yang, R. Tan, X. Wu, Y. Shen, An agglutinate magnetic spray transforms inanimate objects into millirobots for biomedical applications. *Sci. Robot.* **5**, eabc8191 (2020).
- J. Tang, Q. Yin, Y. Qiao, T. Wang, Shape morphing of hydrogels in alternating magnetic field. *ACS Appl. Mater. Interfaces* **11**, 21194–21200 (2019).
- H. Deng, K. Sattari, Y. Xie, P. Liao, Z. Yan, J. Lin, Laser reprogramming magnetic anisotropy in soft composites for reconfigurable 3D shaping. *Nat. Commun.* **11**, 6325 (2020).
- N. Ebrahimi, C. Bi, D. J. Cappelleri, G. Ciuti, A. T. Conn, D. Favier, N. Habibi, A. Hošovský, V. Iacovacci, I. S. M. Khalil, V. Magdanz, S. Misra, C. Pawashe, R. Rashidifar, P. E. D. Soto-Rodriguez, Z. Fekete, A. Jafari, Magnetic actuation methods in bio/soft robotics. *Adv. Funct. Mater.* **31**, 2005137 (2020).
- D.-i. Kim, S. Song, S. Jang, G. Kim, J. Lee, Y. Lee, S. Park, Untethered gripper-type hydrogel millirobot actuated by electric field and magnetic field. *Smart Mater. Struct.* **29**, 085024 (2020).
- Z. Ren, W. Hu, X. Dong, M. Sitti, Multi-functional soft-bodied jellyfish-like swimming. *Nat. Commun.* **10**, 1–12 (2019).
- T. Xu, C. Huang, Z. Lai, X. Wu, Independent control strategy of multiple magnetic flexible millirobots for position control and path following. *IEEE Transactions on Robotics* **38**, 2875–2887 (2022).
- W. Fan, C. Shan, H. Guo, J. Sang, R. Wang, R. Zheng, K. Sui, Z. Nie, Dual-gradient enabled ultrafast biomimetic snapping of hydrogel materials. *Sci. Adv.* **5**, eaav7174 (2019).
- H. W. Huang, M. S. Sakar, A. J. Petruska, S. Pane, B. J. Nelson, Soft micromachines with programmable motility and morphology. *Nat. Commun.* **7**, 12263 (2016).
- S. J. Jeon, R. C. Hayward, Reconfigurable microscale frameworks from concatenated helices with controlled chirality. *Adv. Mater.* **29**, 1606111 (2017).
- C. Ma, X. Le, X. Tang, J. He, P. Xiao, J. Zheng, H. Xiao, W. Lu, J. Zhang, Y. Huang, T. Chen, A multiresponsive anisotropic hydrogel with macroscopic 3D complex deformations. *Adv. Funct. Mater.* **26**, 8670–8676 (2016).
- A. S. Gladman, E. A. Matsumoto, R. G. Nuzzo, L. Mahadevan, J. A. Lewis, Biomimetic 4D printing. *Nat. Mater.* **15**, 413–418 (2016).
- Y. Kim, H. Yuk, R. Zhao, S. A. Chester, X. Zhao, Printing ferromagnetic domains for untethered fast-transforming soft materials. *Nature* **558**, 274–279 (2018).
- Y. Hu, C.-H. Lu, W. Guo, M. A. Aleman-Garcia, J. Ren, I. Willner, A shape memory acrylamide/DNA hydrogel exhibiting switchable dual pH-responsiveness. *Adv. Funct. Mater.* **25**, 6867–6874 (2015).
- J. Kim, C. Kim, Y. Song, S.-G. Jeong, T.-S. Kim, C.-S. Lee, Reversible self-bending soft hydrogel microstructures with mechanically optimized designs. *Chem. Eng. J.* **321**, 384–393 (2017).
- C. Ma, W. Lu, X. Yang, J. He, X. Le, L. Wang, J. Zhang, M. J. Serpe, Y. Huang, T. Chen, Bio-inspired anisotropic hydrogel actuators with on-off switchable and color-tunable fluorescence behaviors. *Adv. Funct. Mater.* **28**, 1704568 (2018).
- C. Yoon, R. Xiao, J. Park, J. Cha, T. D. Nguyen, D. H. Gracias, Functional stimuli responsive hydrogel devices by self-folding. *Smart Mater. Struct.* **23**, 094008 (2014).
- J. Bae, N. P. Bende, A. A. Evans, J.-H. Na, C. D. Santangelo, R. C. Hayward, Programmable and reversible assembly of soft capillary multipoles. *Mater. Horiz.* **4**, 228–235 (2017).
- A. Cangialosi, C. Yoon, J. Liu, Q. Huang, J. Guo, T. D. Nguyen, D. H. Gracias, R. Schulman, DNA sequence-directed shape change of photopatterned hydrogels via high-degree swelling. *Science* **357**, 1126–1130 (2017).
- M. Zhang, Y. Wang, M. Jian, C. Wang, X. Liang, J. Niu, Y. Zhang, Spontaneous alignment of graphene oxide in hydrogel during 3D printing for multistimuli-responsive actuation. *Adv. Sci.* **7**, 1903048 (2020).
- T.-Y. Huang, H.-W. Huang, D. Jin, Q. Chen, J. Huang, L. Zhang, H. Duan, Four-dimensional micro-building blocks. *Sci. Adv.* **6**, eaav8219 (2020).
- A. C. Hernández-González, L. Téllez-Jurado, L. M. Rodríguez-Lorenzo, Alginate hydrogels for bone tissue engineering, from injectables to bioprinting: A review. *Carbohydr. Polym.* **229**, 115514 (2020).

Acknowledgments: We thank Z. Yin, M. Zhang, and T. Wang for assistance in ex vivo experiments and discussions. **Funding:** This work was supported by the National Key R&D Program of China under grant number 2019YFB1309701, the National Natural Science Foundation of China (NSFC) under grant numbers 62222305 and U22A2064, and the Ministry of National Education of the Republic of Turkey. **Author contributions:** Conceptualization: Z.Z., H.W., and M.S. Methodology: Z.Z., H.W., and S.O.D. Investigation: Z.Z. and S.O.D. Simulation: Z.Z. and H.W. Writing—original draft: Z.Z., S.O.D., H.W., Q.H., T.F., and M.S. Writing—review and editing: Z.Z., Q.H., T.F., and M.S. **Competing interests:** The authors declare that they have no competing interests. **Data and materials availability:** All data needed to evaluate the conclusions in the paper are present in the paper and/or the Supplementary Materials.

Submitted 31 August 2022
Accepted 10 November 2022
Published 14 December 2022
10.1126/sciadv.ade6135